A Neural-Network-Based Beamformer for Phased Array Weather Radar

Tarek Sallam, Adel B. Abdel-Rahman, Masoud Alghoniemy, *Senior Member, IEEE*, Zen Kawasaki, *Member, IEEE*, and Tomoo Ushio, *Member, IEEE*

***Abstract*—Phased array weather radars, particularly with high temporal resolution, essentially need a robust and fast beamformer to accurately estimate precipitation profiles such as reflectivity and Doppler velocity. In this paper, we introduce a neural-network-based beamformer to address this problem. In particular, the optimum weight vector is computed by modeling the problem as a three-layer radial basis function neural network (RBFNN), which is trained with I/O pairs obtained from the optimum Wiener solution. The RBFNN was chosen because of its characteristic of accurate approximation and good generalization, and its robustness against interference and noise. The proposed RBFNN beamforming method is compared with traditional beamforming methods, namely, Fourier beamforming (FR), Capon beamforming, and the flower pollination algorithm (FPA), which is a recently proposed nature-inspired optimization algorithm. It is shown that the RBFNN approach has nearly optimal performance in various precipitation radar signal simulations relative to the rival methods. The validity of the RBFNN beamformer is demonstrated by using real weather data collected by the phased array radar (PAR) at Osaka University, and compared with, in addition to the FR and FPA methods, the minimum mean square error beamforming method. It is shown that the RBFNN method estimates the reflectivity of the PAR at Osaka University with less clutter level than those of the other three methods.**

***Index Terms*—Evolutionary optimization, phased array digital beamforming (DBF), radial basis function (RBF) neural networks, weather radar.**

I. Introduction

THE development of high-speed phased array weather radars (PARs) with rapid and accurate detection of weather phenomena is an important topic of current research interest. Recently, PARs have demonstrated high time-resolution and high-precision estimation of Doppler velocity and reflectivity of precipitation compared with the mechanically scanning radar. PARs use electronic scanning to rapidly collect radar measurements: The mobile rapid scanning X-band polarimetric Doppler radar [1], the atmospheric imaging radar [2], and the airborne polarimetric Doppler weather radar [3] are examples of PARs in meteorological applications. We should also include the National Weather Radar Testbed, which is being evaluated as a multifunction PAR [4].

Fig. 1. Photographs of the PAR at Suita campus at Osaka University. The right photograph shows the 128-element antenna array of the PAR system inside the radar dome of the left photograph.

Osaka University and Toshiba Corporation have started developing a new PAR at X-band [5] under the grant of the Japanese National Institute of Information and Communications Technology in 2007, and installed at Osaka University, Osaka, Japan, in 2012 mainly for operational purposes. This new PAR system (see Fig. 1) has the unique capability of scanning the whole sky with 100 m and 10–30 s resolution up to 60 km. The system adopts the digital beamforming (DBF) technique for elevation scanning with 100 elevation angles and mechanically rotates the array antenna in azimuth direction with 1° resolution within 10–30 s. The radar transmits a broad beam of several degrees (fan beam) with 24 antenna array elements and receives and digitizes the back scattered signal at 128 array elements; then, by digitally forming the received beam, fast scanning is realized.

A significant problem with fan beam transmission is the huge sidelobes of strong echoes from strong precipitation cells or clutter, which are almost two times stronger than a sharp beam transmission and reception in decibels. For example, while a sharp beam transmission and reception has a first sidelobe level of −27 dB from the main lobe for the center direction, as in the case with the Colorado State University–University of Chicago–Illinois State Weather Survey (CSU-CHILL) radar

Manuscript received November 9, 2015; revised March 19, 2016; accepted April 3, 2016. Date of publication May 4, 2016; date of current version August 2, 2016. This work was supported in part by the Japan Science and Technology Agency through the Cross-ministerial Strategic Innovation Promotion Program and in part by the Japan Society for the Promotion of Science through the KAKENHI program.

T. Sallam is with the Faculty of Engineering at Shoubra, Banha University, Cairo 11241, Egypt (e-mail: tarek.sallam@feng.bu.edu.eg).

A. B. Abdel-Rahman is with the Faculty of Engineering, South Valley University, Qena 83523, Egypt, and also with Egypt–Japan University of Science and Technology, Alexandria 21934, Egypt (e-mail: adel_b15@eng.svu.edu.eg).

M. Alghoniemy is with the Department of Electrical Engineering, University of Alexandria, Alexandria 21544, Egypt (e-mail: alghoniemy@alexu.edu.eg).

Z. Kawasaki was with Osaka University, Osaka 565-0871, Japan (e-mail: zen@comm.eng.osaka-u.ac.jp).

T. Ushio is with Osaka University, Osaka 565-0871, Japan (e-mail: ushio@comm.eng.osaka-u.ac.jp).

Color versions of one or more of the figures in this paper are available online at http://ieeexplore.ieee.org.

Digital Object Identifier 10.1109/TGRS.2016.2554116

[19], which has a normal parabolic dish antenna, a configuration of uniform and sharp beams has a first sidelobe level of -13 dB in the same angle. Consequently, observations from the PAR systems often show the received signal is seriously contaminated by relatively high power from ground clutter through the sidelobes of the broad transmitting beam.

Several adaptive DBF methods have been proposed for clutter mitigation in a PAR system. In particular, in atmospheric radars, the Capon beamforming (CP) method has been used extensively [6], [7]; the Capon method requires a sufficient number of pulses to produce reasonable results and cannot work well with 16 pulses as in the PAR. A beamformer based on a recursive implementation of the minimum mean square error (MMSE) framework, with a unity gain constraint in the lock direction, has been developed in [8]. The MMSE method offers sidelobe reduction and accurate estimation for point and distributed targets with fewer pulses on the PAR; however, for small ranges of elevation angles, it does not converge and consequently gives bad results particularly on real data PAR.

On the other hand, neural networks [9] are gaining a huge momentum in the field of signal processing [10] mainly because of its generalization capability, nonlinear property, massive parallelism, adaptive learning capability, fast convergence rates, insensitivity to uncertainty, and VLSI implementations. In particular, neural networks have shown to successfully classify complex data and perform function approximation for many remote sensing problems. For example, in [11], neural networks is used for cloud classification, in [12], for the retrieval of atmospheric temperature and moisture profiles, and in [13] for rainfall estimation, to name a few.

Motivated by the inherent advantages of the neural network, this paper proposes the development of a radial-basis-function neural network (RBFNN)-based approach to the beamforming of PAR using both simulated and real data. Neural networks typically adopt two steps: training and recalling. The network is first trained with known input–output pattern pairs; although a large training pattern set may be required for network training, it can be implemented offline. After training, it can be used directly to replace the complex system dynamics. In this paper, the RBFNN is trained on the optimum weights of Wiener solution. The RBFNN has shown an excellent performance in estimating point and distributed targets, irrespective of the number of used pulses in the PAR, compared to the traditional Fourier beamforming (FR), Capon methods, and the flower pollination algorithm (FPA). Moreover, when operated on real data, collected by the PAR at Osaka University (PAR@OU), the RBFNN method estimates radar reflectivity with less clutter than the FR, FPA, and MMSE methods.

This paper is organized as follows. In Section II, the signal model of PAR and the development of RBFNN for the PAR beamforming problem are introduced. Both FR and the FPA are introduced and used for performance comparisons. In Section III, estimation accuracy values of these three methods, in addition to the Capon method, are evaluated and compared, using signals generated by the precipitation radar signal simulator. Moreover, a quantitative comparison about the beamforming speed among the mentioned methods is given. In Section IV, estimation results for precipitation for RBFNN, FR, FPA, and MMSE methods are illustrated with the use of real data collected by PAR@OU. Conclusions are summarized in Section V.

II. Methodology

A. Signal Model

Assuming a uniform linear phased array antenna with N elements, the lth time sample of the received $N \times 1$ complex amplitude $\mathbf{x}_l$ is expressed by an associated $M \times 1$ complex amplitude $\mathbf{s}_l$ in an arbitrary range bin, i.e., an $N \times M$ matrix $\mathbf{A}$ that consists of the spatial steering vectors $\mathbf{a}(\theta_m)$, $m = 0, 1, \ldots, M-1$, the additive Gaussian noise $\mathbf{n}_l$ as

$$\mathbf{x}_l = \mathbf{A}\mathbf{s}_l + \mathbf{n}_l \tag{1}$$

where

$$\mathbf{x}_l = [x_{l,0}\ x_{l,1}\ \cdots\ x_{l,N-1}]^T \tag{2}$$

$$\mathbf{s}_l = [s_{l,0}\ s_{l,1}\ \cdots\ s_{l,M-1}]^T \tag{3}$$

$$\mathbf{A} = [\mathbf{a}(\theta_0)\ \mathbf{a}(\theta_1)\ \cdots\ \mathbf{a}(\theta_{M-1})] \tag{4}$$

$$\mathbf{a}(\theta_m) = [1\ \exp(-j\beta_1(\theta_m))\ \cdots\ \exp(-j\beta_{N-1}(\theta_m))]^T \tag{5}$$

$$\beta_n(\theta_m) = (2\pi/\lambda)\ dn\ \sin(\theta_m) \tag{6}$$

where $[\cdot]^T$ is the transpose operator, λ is the wavelength, and d is the spacing between any two adjacent antenna elements. In the PAR settings, θ_m is the elevation angle, and $\mathbf{s}_l$ corresponds to the M-separated precipitation profiles in elevation angles. The estimated precipitation profiles $\mathbf{y}_l = [y_{l,0}\ y_{l,1}\ \cdots\ y_{l,M-1}]^T$ are calculated as

$$y_{l,m} = \mathbf{w}_m^H \mathbf{x}_l \tag{7}$$

where $\mathbf{w}_m$ is the $N \times 1$ complex array weights that correspond to the elevation angle m, and $[\cdot]^H$ is the complex conjugate transpose.

B. Wiener Solution

Consider a reference signal $d_{l,m}$, which is either identical to or highly correlated with the desired signal $s_{l,m}$ and is uncorrelated with the signals coming from the other directions. Define the error signal $\varepsilon_{l,m}$ as [14]

$$\varepsilon_{l,m} = d_{l,m} - y_{l,m} \tag{8}$$

substituting from (7) into (8), we obtain

$$\varepsilon_{l,m} = d_{l,m} - \mathbf{w}_m^H \mathbf{x}_l. \tag{9}$$

For the purpose of simplification, we will suppress the subscripts l and m and insert them in the final solution [14]. Squaring (9), we have

$$|\varepsilon|^2 = |d|^2 - 2d\mathbf{w}^H\mathbf{x} + \mathbf{w}^H\mathbf{x}\mathbf{x}^H\mathbf{w}. \tag{10}$$

Taking the expected value of both sides and simplifying the expression, we obtain the MSE as follows:

$$E\left[|\varepsilon|^2\right] = E\left[|d|^2\right] - 2\mathbf{w}^H\mathbf{r} + \mathbf{w}^H\mathbf{R}_x\mathbf{w} \tag{11}$$

where $\mathbf{r}$ is the cross correlation between the reference and the observation signals, and $\mathbf{R}$ is the autocorrelation matrix of the

observation $\mathbf{x}$; the two are defined as follows:

$$\mathbf{r} = E[d\mathbf{x}] \tag{12}$$

$$\mathbf{R}_x = E[\mathbf{x}\mathbf{x}^H]. \tag{13}$$

It should be noted that the MMSE solution is the result of minimizing (11).

In general, for an arbitrary number of weights, one can find the minimum value by taking the gradient of the MSE with respect to the weight vectors and equating it to zero. Thus, the Wiener–Hopf equation is given by [14]

$$\nabla_{\mathbf{w}} \left(E \left[|\varepsilon|^2 \right] \right) = 2\mathbf{R}_x \mathbf{w} - 2\mathbf{r} = 0 \tag{14}$$

yielding the optimum Wiener solution as

$$\mathbf{w}_{\text{Wiener}} = \mathbf{R}_x^{-1} \mathbf{r}. \tag{15}$$

If we allow the reference signal $d_{l,m}$ to be equal to the desired signal $s_{l,m}$ and if $s_{l,m}$ is uncorrelated with all other signals, one may simplify the correlation $\mathbf{r}$. Using (12), the simplified correlation $\mathbf{r}$ is

$$\mathbf{r} = E \left[s_{l,m}^* \cdot \mathbf{x}_l \right] = s_m \cdot \mathbf{a}(\theta_m) \tag{16}$$

where

$$s_m = E \left[|s_{l,m}|^2 \right] = \frac{1}{L} \sum_{l=1}^{L} s_{l,m} s_{l,m}^* \tag{17}$$

L is the number of time samples. Now, the optimum weights can then be identified as [14]

$$\mathbf{w}_{\text{Wiener}}^m = s_m \mathbf{R}_x^{-1} \mathbf{a}(\theta_m). \tag{18}$$

C. Fourier Beamforming

The Fourier beamformer, also known as the matched filter, is the most basic beamformer in PARs for steering a beam in a certain direction by uniforming the phase shift. In particular, the array weights vector can be expressed as [8]

$$\mathbf{w}_{\text{FR}}^m = \frac{\boldsymbol{a}(\theta_m)}{N}. \tag{19}$$

D. Flower Pollination Algorithm

The FPA is a recently invented evolutionary optimization algorithm inspired from the flower pollination process of flowering plants [15]. The main purpose of a flower is ultimately reproduction via pollination. Flower pollination is typically associated with the transfer of pollen, and such transfer is often linked with pollinators such as insects, birds, bats, and other animals. Pollination can be achieved by self-pollination or cross pollination. Cross pollination, or allogamy, means pollination can occur from pollen of a flower of different plants, whereas self-pollination is the fertilization of one flower, such as peach flowers, from pollen of the same flower or different flowers of the same plant, which often occurs when there is no reliable pollinator available. Biotic cross-pollination may occur at long distance, and the pollinators such as bees, bats, birds, and flies can fly a long distance; thus, they can be considered the global pollination. In addition, bees and birds may behave in accordance to the Lévy flight behavior [16], with jump or fly distance steps obeying a Lévy distribution. Furthermore, flower constancy can be used as an increment step using the similarity or difference of two flowers.

In [15], the above characteristics of the pollination process, flower constancy, and pollinator behavior are idealized in the following four rules: 1) biotic pollination and cross-pollination are considered global pollination processes with pollen-carrying pollinators performing Lévy flights; 2) abiotic and self-pollination are considered as local pollination; 3) flower constancy can be considered the reproduction probability that is proportional to the similarity of two involved flowers; and 4) local and global pollination are controlled by a probability switch $p \in [0, 1]$.

Due to the physical proximity and other factors such as wind, local pollination can have a significant fraction p in the overall pollination activities. In the global pollination step, flower pollens are carried by pollinators such as insects, and pollens can travel over a long distance. This ensures the pollination and reproduction of the fittest; thus, we represent the most fittest as $\mathbf{g}$. The first rule can then be formulated as [15]

$$\mathbf{w}_i^{t+1} = \mathbf{w}_i^t + V \left(\mathbf{w}_i^t - \mathbf{g} \right) \tag{20}$$

where $\mathbf{w}_i^t$ is the solution vector, i.e., pollen i at iteration t, $\mathbf{g}$ is the current best solution, and V is the strength of the pollination, which is a step size randomly drawn from Lévy distribution. The local pollination (Rule 2) can be represented as

$$\mathbf{w}_i^{t+1} = \mathbf{w}_i^t + \gamma \left(\mathbf{w}_j^t - \mathbf{w}_k^t \right) \tag{21}$$

where $\mathbf{w}_j^t$ and $\mathbf{w}_k^t$ are pollens from different flowers of the same plant species. The parameter γ is drawn from uniform distribution in the range between zero and one.

In this paper, the FPA is used to minimize the cost function in (11) using 100 iterations (per elevation angle) to get the optimum weights $\boldsymbol{w}_{\text{FPA}}$. The switch probability p is chosen to be 0.8, and the population size is 25.

E. RBFNN Beamformer

The Wiener weight vector $\mathbf{w}_{\text{Wiener}}$ in (18) is not suitable for real-time implementation in its current format. Therefore, it can be approximated using a suitable architecture such as the RBFNN. The array outputs are preprocessed, and then applied to the RBFNN, where $\mathbf{R}_x$ is fed to the input layer of the RBFNN, and the vector $\widehat{\mathbf{w}}_{\text{Wiener}}$ is generated at the output layer as an estimate of the Wiener weight vector. As it is the case with most neural networks, the RBFNN is designed to perform an input–output mapping trained with M precipitation profiles or elevation angles $(\mathbf{R}_x^m; \mathbf{w}_{\text{Wiener}}^m)$, $m = 0, 1, \ldots, M-1$ [17].

1) RBFNN Model: The RBFNN is a special three-layer feed-forward network, which consists of an input layer, an output layer, and a hidden layer as shown in Fig. 2. In the hidden layer, the nonlinear functions are usually considered Gaussian functions of appropriately chosen means and variance. The weights from the hidden to the output layer are determined by considering a supervised learning procedure. Assume that the

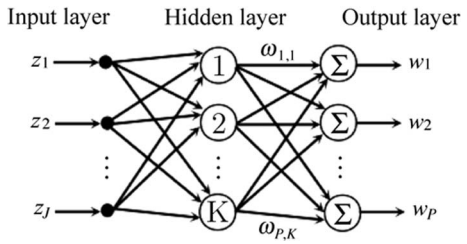

Fig. 2. Architecture of the RBFNN.

input, hidden, and output layers have J, K, P nodes, respectively. The network output vector is given by

$$w_p = \sum_{k=1}^{K} \omega_{p,k} e^{-\frac{\|\mathbf{z}-\mathbf{c}_k\|^2}{\sigma_k^2}} \quad (p = 1, \ldots, P) \tag{22}$$

where $\mathbf{z} = [z_1 \ z_2 \ \cdots \ z_J]$ is the input vector to the network, $\mathbf{c}_k$ and σ_k are the center vector and the standard deviation (spread parameter) of the kth Gaussian function, respectively, and $\{\omega_{p,k}; p = 1, \ldots, P; k = 1, \ldots, K\}$ is the weight from the kth hidden node to pth output node.

2) Generation of Training Data: To reduce the training time of the RBFNN, a fast training approach is adopted from [17] in which only either the upper or lower triangular part (excluding the main diagonal) of the correlation matrix $\mathbf{R}_x$ is considered. In this case, an $N \times N$ correlation matrix $\mathbf{R}_x$ is rearranged in an $N(N-1)/2$ component input vector as

$$\mathbf{b} = \left[R_{12}, R_{13}, \ldots, R_{1,N}; R_{23}, \ldots, R_{2,N}; \ldots; R_{(N-1),N}\right]. \tag{23}$$

Note that the network needs twice as many input nodes since it does not deal with complex numbers; therefore, the total number of input nodes is $N(N-1)$. The input vector is then normalized by its norm to unify the input parameter space, i.e.,

$$\mathbf{z} = \frac{\mathbf{b}}{\|\mathbf{b}\|} \tag{24}$$

producing the required training input/output pairs of the training set, i.e., $(\mathbf{z}^m; \mathbf{w}^m_{\text{Wiener}})$, $m = 0, 1, \ldots, M-1$. Once the RBFNN is trained with a representative set of training input/output pairs, it is ready to function in the performance and recalling phases. In the performance phase, the trained network can be directly used to produce optimum weights for the real-time PAR beamformer [17].

3) Performance Phase of the RBFNN: After the training phase is complete, the RBFNN should have established an approximation of the desired input/output mapping. In the recalling phase, the neural network is expected to generalize, i.e., responds to inputs that have never been seen before but are drawn from the same input distribution that is used in the training set. The procedure of the performance phase is summarized in the following simple steps.

1) Rearrange the correlation matrix into vector $\mathbf{z}$ as in (23) and (24).
2) Present vector $\mathbf{z}$ at the input layer of the trained RBFNN; the output layer of the trained RBFNN will produce $\mathbf{w}_{\text{RBFNN}}$ $(\widehat{\mathbf{w}}_{\text{Wiener}})$ as an estimate to the optimum Wiener weight vector of (18).

TABLE I
CHARACTERISTICS OF RADAR SIGNAL SIMULATION

Parameter	Value
Frequency	9.4 GHz
Number of antenna elements (N)	128
Spacing between adjacent antenna elements (d)	16.5 mm
Tilt angle of antenna	30°
Pulse repetition frequency	5.4 KHz
Number of pulses (L)	16
Number of elevation angles (M)	1201 (-30° to 90° with step 0.1°)

In this paper, the RBFNN is trained using the MATLAB training function `newrb`, in which a hidden node is added each epoch (iteration) until a target MSE is reached.

III. Simulation Results

The performance of RBFNN beamforming is evaluated and compared with both the FR and FPA methods via radar signal simulations. Simulation signals were generated by a procedure described by Chandrasekar *et al.* [18] that generates a time series of received signals having a Gaussian spectral shape. The elevation profile of power corresponding to $\mathbf{s}$ is determined at each simulation model; then, the received signals $\mathbf{x}$ are calculated using (1) with additive Gaussian noise. Here, each antenna element is assumed omnidirectional. The parameters of this simulation are shown in Table I, the frequency, number of antenna elements, spacing of adjacent antenna elements, tilt angle of the antenna, and pulse repetition frequency are designed parameters of PAR@OU operating at about 16 pulses. A wide range of elevation angles from $-30°$ to $90°$ is considered. Since the PAR@OU transmits a fan beam with -3-dB beamwidth of about $10°$, we may deal with a narrower range of elevation angle, which gives us less computational cost. It should be noted that the fan beam is not considered in this paper because the beamformer processes only the receiver side and not the transmitted signal. Additionally, the simulation with this wide range of elevation angles obviously shows the difference among methods of comparison.

A. Estimation of Point Targets

Here, point targets, such as aircraft, are estimated using the FR, FPA, and RBFNN methods and compared with the true values. In Fig. 3(a), an example of the mean power estimates for two point targets is shown; it is assumed that the two targets are placed at elevations of $25°$ and $35°$, respectively, in the same range, and azimuth bin with mean received power of 15 and 45 dB, and mean Doppler velocities of 8 and 10 m/s, as indicated by the black circles. The white noise is assumed to be about 10 dB. The estimated results of the two elevations are summarized in Table II, it should be noted that the true values do not strictly agree with the input parameters indicated earlier because the radar signal simulator provides random values. On the other hand, the FR correctly estimates the received power of the right (strong) target; however, it has the poorest resolution and the highest sidelobes. The received power of the left (weak) target is overestimated by about 0.4 dB by the sidelobes of the right target. The FPA detects both targets with optimal resolution (no sidelobes); it correctly estimates the right target while overestimating the left target by only 0.05 dB. The

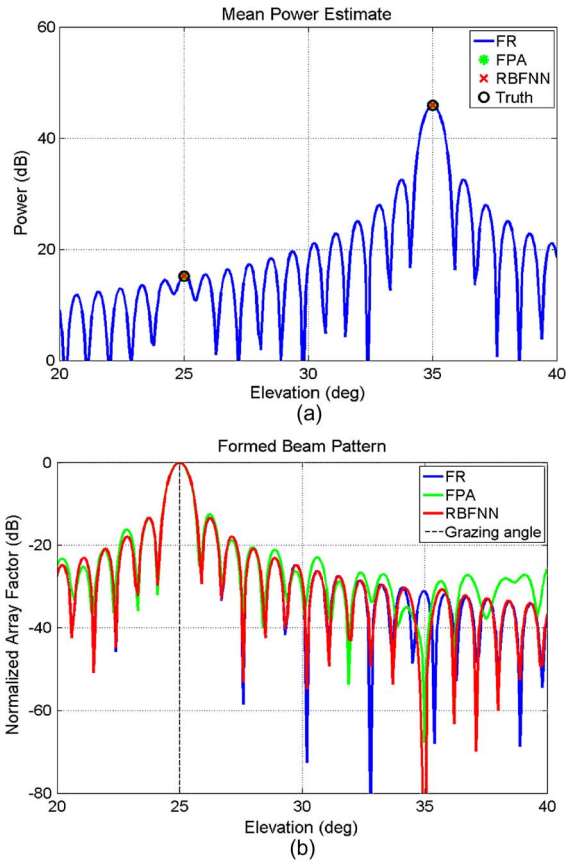

Fig. 3. Estimation of point targets. (a) Mean power estimates for two targets placed at elevations of 25° and 35°. (b) Formed beam pattern grazing at an elevation angle of 25°.

TABLE II
MEAN POWER ESTIMATES FOR THE POINT TARGETS

Approach	Left Target (dB)	Right Target (dB)
Truth	15.16	45.89
RBFNN	15.16	45.89
FPA	15.21	45.89
FR	15.56	45.89

TABLE III
BIAS ERROR OF MISSING POINT TARGETS IN RBFNN TRAINING

Missing Target	Bias Error (dB)
Left target	0.0918
Right target	0.0564
Both targets	0.1525 for left and -0.0709 for right

RBFNN shows also optimal resolution with no sidelobes but gives the optimal power estimation results for both the targets that agree exactly with the truth. In Fig. 3(b), the formed beam patterns of each method for an elevation of 25° are shown. FPA and RBFNN form a null at an elevation of 35°. This is why detection and power estimates of the left target are not much affected by the right target in these methods, unlike in the FR. Note also that the RBFNN has a deeper null at 35° compared with the FPA, which provides more accurate estimate, the same as the truth value, at the 25° target.

The question now is how the NN behaves when it encounters inputs that are drawn from a different distribution than the one used in the training set. This can be checked by letting either of the targets to be missing or both targets be missing in the training phase. Table III shows the bias errors in these

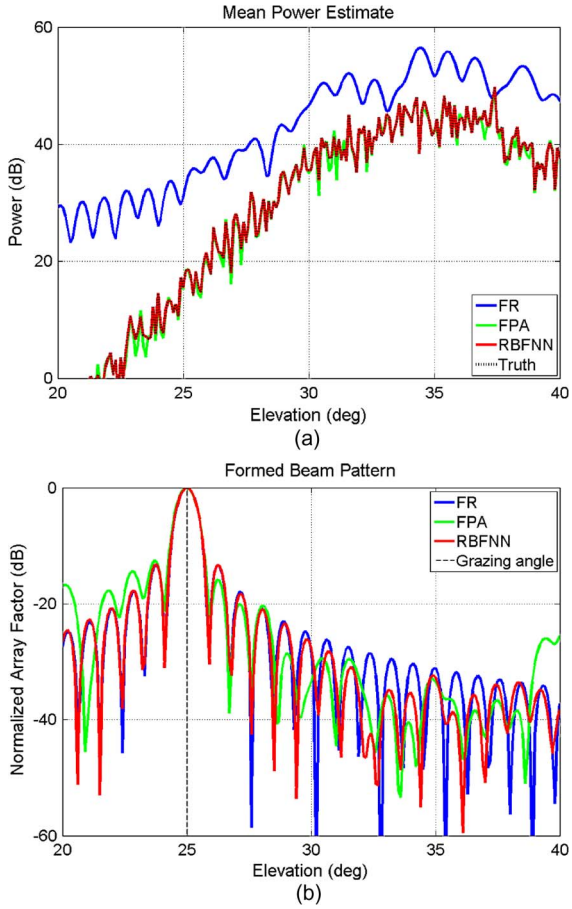

Fig. 4. Estimation of distributed targets for one-cell precipitation. (a) Mean power estimate. (b) Formed beam pattern grazing at an elevation angle of 25°.

cases (the bias error is defined as the difference between the estimated power and the correct power in decibels). When the left target is missing, the RBFNN is trained at 25.1° and tested at 25°. If the right target is missing, the network is trained at 35.5° and tested at 35°. If both targets are missed, a third middle target is added at 30° of power 35 dB. We can conclude from Table III that the RBFNN leads to small bias errors when tested at elevations not encountered in the training phase.

B. Estimation of Distributed Targets

1) One Precipitation Cell: In Fig. 4(a), an example of the mean power estimates for one-cell distributed targets is shown. The mean power of additional white noise is assumed to be about 10 dB. It can be seen that the FR consistently overestimates the truth getting closer to it as the elevation increases. Moreover, we can see that the RBFNN correctly estimates the mean power better than the FPA. As shown in Fig. 4(b), both the FPA and the RBFNN suppress sidelobes adaptively.

To show the robustness of the RBFNN beamformer, it has been tested with inputs that have never been seen during the training phase; consequently, this also validates its generalization capability. Fig. 5 shows the estimation of one-cell distributed target in which the RBFNN is tested with 0.1° step in elevation while trained with 0.3° and 0.5° elevation step. It can be seen that the network has very good agreement with the truth

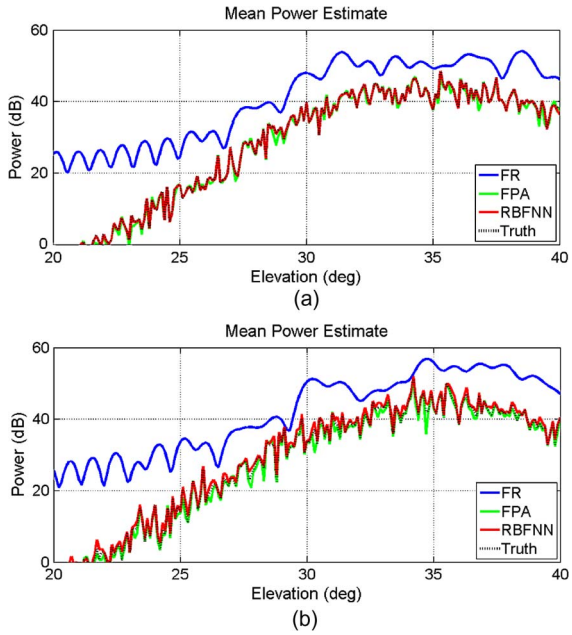

Fig. 5. Estimation of one-cell distributed target with RBFNN tested at 0.1° elevation step and trained with an elevation step of (a) 0.3° and (b) 0.5°.

in case of 0.3° step training while having little overestimations in 0.5° step training case.

2) Two Precipitation Cells: The estimation accuracy values of these methods are compared in mean power by the radar signal simulation assuming distributed targets with two precipitation cells. Example of the mean power estimate is shown in Fig. 6(a). The mean power estimate of these methods is calculated with the use of the most general methods based on a time series, which is elaborated in [19, Ch. 5 (5.10)]. As shown in Fig. 6(a), the FR shows high sidelobes in mean power estimates and correctly estimates them only around the peaks, in which strong distributed targets exist; the FPA gives better results but with little underestimation. It is obvious that the RBFNN has superior performance over the other two methods. The elevation–Doppler velocity spectrographs shown in Fig. 7 are very helpful for understanding the characteristics of these methods. In particular, in Fig. 7(a), it is shown that signals contaminate each other by their sidelobes in the FR method. However, the FPA gives little underestimation with much suppression of sidelobes. Compared with both the FR and the FPA, the spectrograph of RBFNN is very similar to that of the truth.

It should be noted that the PAR is designed to detect precipitation in urban areas in which it is anticipated that strong ground clutter and its sidelobes significantly contaminate the desired signals. Ground clutter appears at elevations in which ground, trees, or buildings exist in a desired range bin. The estimated results are evaluated with the addition of ground clutter signals. The ground clutter elements have a mean power of a Gaussian shape whose peak is positioned at 0° elevation with about 110 dB peak power [see Fig. 6(b)]; their mean Doppler velocities are 0 m/s in all the elevations. This clutter signal is also generated by the radar signal simulator stated earlier. In Fig. 6(b), it can be seen that FR has too large sidelobes to detect the distributed signals, and the FPA has little underestimation with sidelobe suppression. RBFNN correctly suppresses the

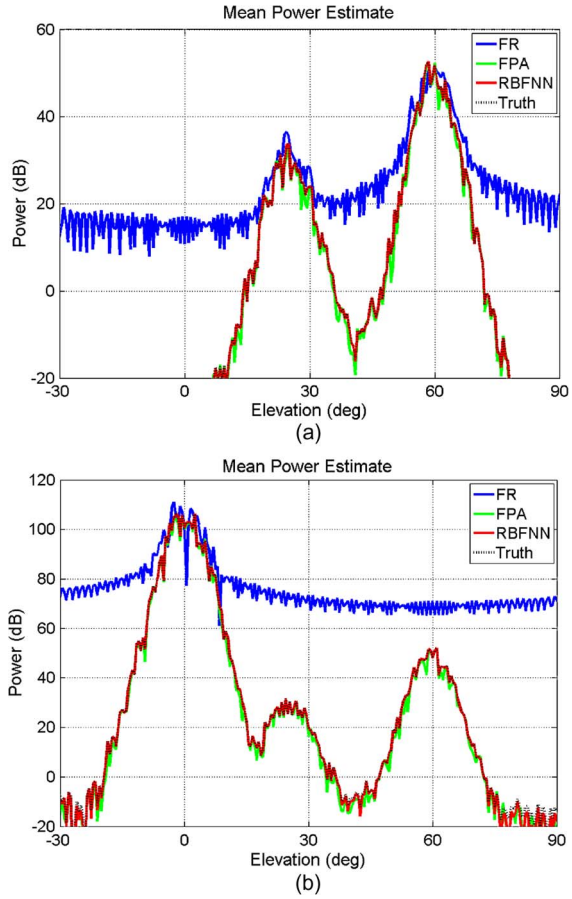

Fig. 6. Mean power estimates of distributed targets for two-cell precipitation. (a) Without clutter. (b) With a clutter of about 110 dB peak power at 0° elevation.

sidelobes of the strong ground clutter and lets the distributed signals appear. Fig. 7(b) shows the elevation–Doppler velocity spectrographs of Fig. 6(b). The characteristics of RBFNN training of all the given simulations, using the `newrb` Matlab training function, are summarized in Table IV.

To test its generalization, the RBFNN is trained at 0.5° elevation step but is tested at 0.1° step. Fig. 8 shows the two-cell distributed target in this case. It can be seen that the RBFNN can predict the precipitation profile quiet fairly even if it is tested with angles never saw in the training.

C. Beamforming Speed

Beamforming speed of the beamformer methods is defined here as the computational complexity of the method which is defined as the execution or CPU time of each method. The average simulation time per elevation angle was 45 μs, 0.08 s, and 0.4 s, for the FR, RBFNN, and FPA algorithms, respectively. Note that the total CPU time is the time taken per elevation angle multiplied by the total number of elevation angles used in the simulation. Moreover, note that the execution time of RBFNN does not include the training time (because training is usually performed offline). From the average simulation time, it is clear that FR is the fastest beamformer; however, it gives bad results compared with the FPA and the RBFNN. Moreover, we can see that the RBFNN is five times faster than the FPA.

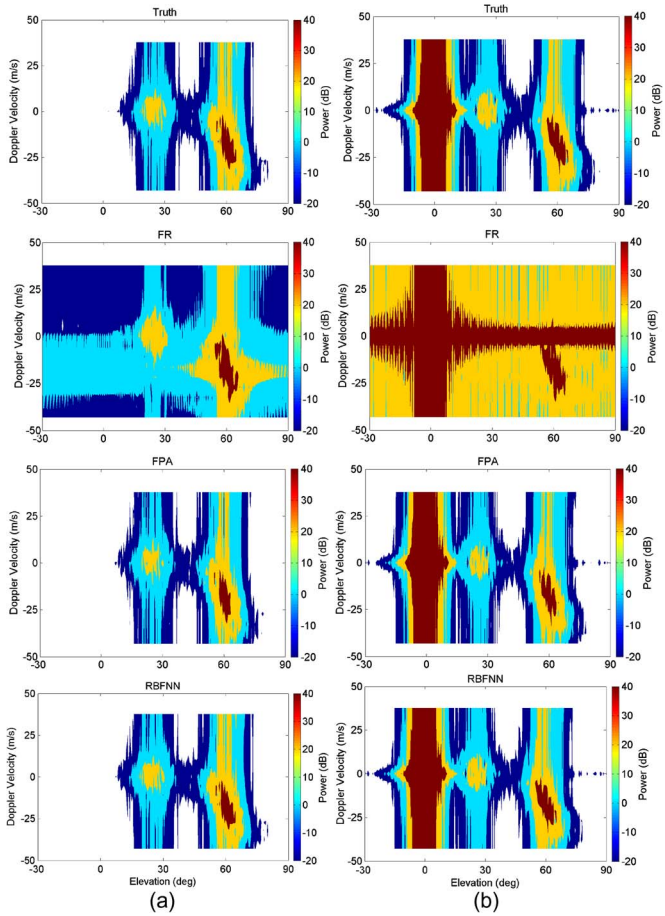

Fig. 7. Elevation–Doppler velocity spectrographs of (a) Fig. 6(a) and (b) Fig. 6(b).

TABLE IV
CHARACTERISTICS OF RBFNN TRAINING FOR NUMERICAL SIMULATION

Characteristic	Point targets	Distributed targets		
		One cell	Two cells	
			Without clutter	With clutter
Goal MSE	1.0E-7	1.0E-7	1.0E-5	5.0E-6
Spread parameter	1	1	0.1	0.1
Training time (s)	5	50	260	400
Number of epochs (hidden nodes)	2	65	140	190

D. Comparison With Capon Beamformer

1) Capon Beamforming: In the CP method, the received power is minimized with a unity gain constraint in the lock direction [14]. In CP, the array weights are given by

$$\mathbf{w}_{\mathrm{CP}}^{m} = \frac{\mathbf{R}_x^{-1}\mathbf{a}(\theta_m)}{\mathbf{a}^H(\theta_m)\mathbf{R}_x^{-1}\mathbf{a}(\theta_m)}. \tag{25}$$

2) Point and Distributed Targets: The CP is compared with the FR, FPA, and RBFNN methods using the same radar signal simulator discussed earlier. Although 256 pulses are not transmitted in the PAR observation, this simulation is carried out to make a comparison with CP, which is not appropriate with a small number of pulses. Fig. 9(a) shows the mean power estimates for two point targets using the four methods.

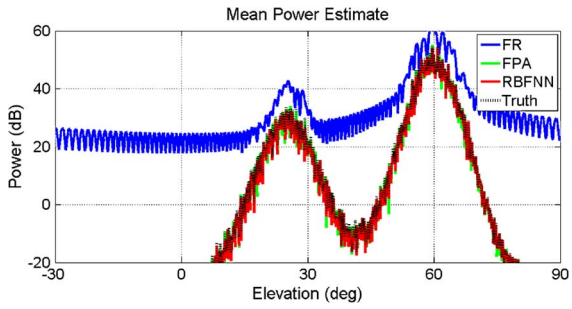

Fig. 8. Estimation of two-cell distributed target with RBFNN trained at 0.5° elevation step and tested at 0.1° step.

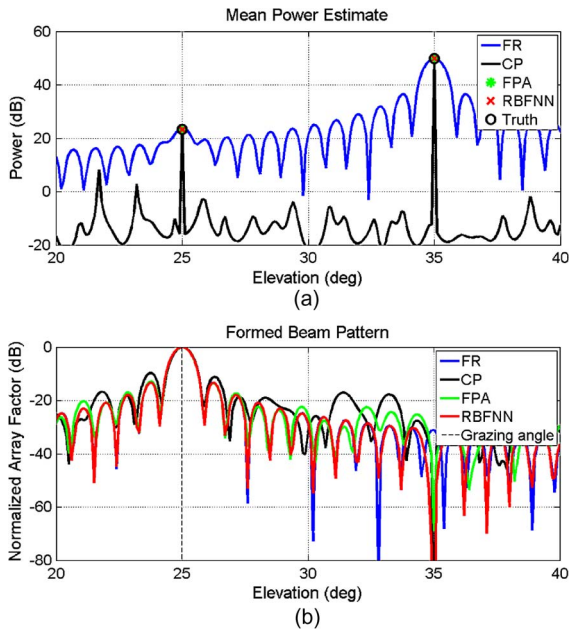

Fig. 9. Estimation of point targets and formed beam pattern for FR, CP, FPA, and RBFNN.

TABLE V
BIAS ERROR IN POINT-TARGET ESTIMATION FOR FR, CP, FPA, AND RBFNN

Approach	In Left Target (dB)	In Right Target (dB)
RBFNN	0.0021	1.6946E-5
FPA	-0.0334	-2.3544E-4
FR	0.5490	-0.0021
CP	1.3487	1.3116

Table V shows the bias error at two targets in each method, where the RBFNN has the smallest bias error among all methods, whereas the CP has the largest bias error. Although the CP correctly detects both targets with high resolution and sufficiently suppresses sidelobes under the noise level, both received power values are overestimated, by about 1.35 and 1.31 dB for the left and right targets, respectively. This overestimation is caused by the correlation between both signals (it is well known that CP works when received signals are independent).

In Fig. 9(b), the formed beam patterns of each method for an elevation of 25° are shown. Although CP forms a null at an elevation of 35°, it has the highest maximum sidelobe level of −9.72 dB, whereas all other methods have almost the same maximum sidelobe level at about −13 dB. It is clear that the

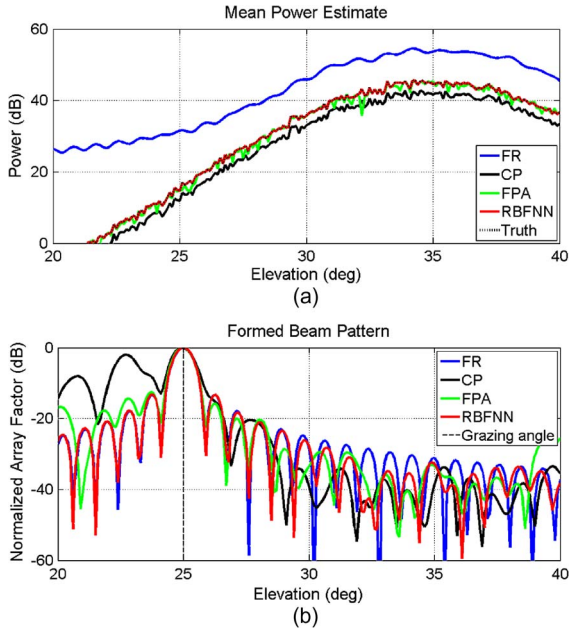

Fig. 10. Estimation of one-cell distributed target and formed beam pattern for FR, CP, FPA, and RBFNN.

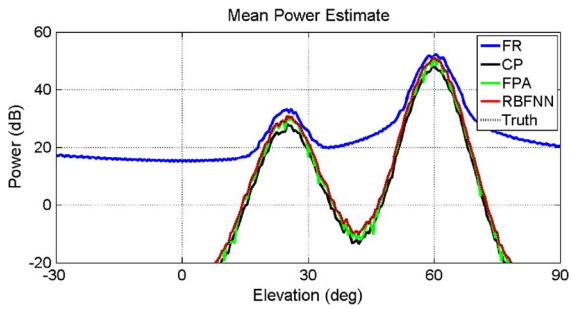

Fig. 11. Estimation of two-cell distributed target for FR, CP, FPA, and RBFNN.

beamwidths of all methods are almost equivalent. This means that these beamforming methods never sharpen main lobes, which are essentially determined by antenna size and only suppress sidelobes adaptively.

In Fig. 10(a), the mean power estimates for one-cell distributed target are shown for the four methods. As shown, CP underestimates, caused by correlations between signal mean power in all elevations. Although the CP solutions get closer to the truth with more pulses as in the point-target simulation, this characteristic of the CP beamformer is a serious problem for precipitation radars because the distributed targets change continuously and a correlation between narrow-band random signals with similar frequencies is high. As shown in Fig. 10(b), although CP beamformer suppresses sidelobes adaptively, as the case with the FPA and RBFNN, it has the highest sidelobe level of about -2 dB, whereas all other methods have also the same sidelobe level at about -13 dB. As in the point-target simulation, the main lobes are not sharpened for distributed targets.

Fig. 11 shows the mean power estimates assuming a distributed target of two precipitation cells. Note that, in Fig. 6(a), where 16 pulses are used, CP has too large underestimation and is not described in the plot range. As shown in Fig. 11, the CP results are better with a larger number of pulses. However,

TABLE VI
MEAN BIAS ERROR IN TWO-CELL DISTRIBUTED TARGET ESTIMATION FOR FR, CP, FPA, AND RBFNN

Approach	For 16 Pulses (dB)	For 256 Pulses (dB)
RBFNN	-0.1	-0.04
FPA	-1.8	-1.23
FR	17.86	15.01
CP	-203.35	-3.1

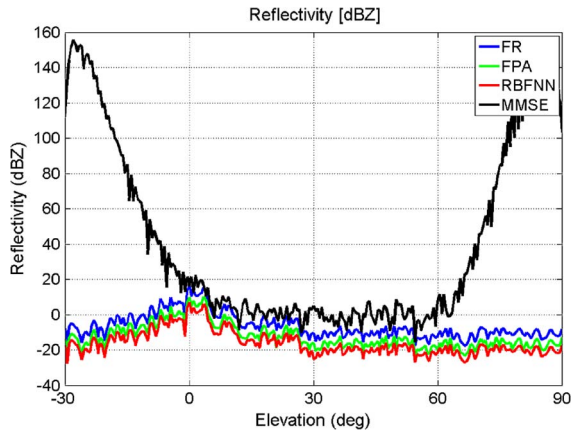

Fig. 12. Reflectivity of PAR@OU at the first range bin and 0° azimuth for a range of elevation from $-30°$ to 90°.

underestimation still remains. Table VI shows the mean bias error of the four methods with 16 and 256 pulses for the estimation of the two-cell distributed target of Figs. 6(a) and 11, respectively. The mean bias error is the bias error averaged over all elevation angles. It can be seen that RBFNN has the least bias error among all methods then comes FPA whether for 16 or 256 pulses. CP cannot output valid results with 16 pulses. Since mean power estimate has large negative bias error less than -200 dB, with 256 pulses, the CP results are much improved even over FR. It can be concluded that the estimation accuracy values of FR, FPA, and RBFNN methods are almost independent on the number of pulses, in contrast to CP.

IV. APPLICATION TO THE PAR@OU

Here, data collected by the PAR@OU were used to evaluate the performance of the FR, MMSE, FPA, and RBFNN methods. The PAR@OU data provide a more realistic profile of precipitation, which is not described in the former simulations; data were collected in a rainy day on September 2, 2013. When applied on PAR@OU, the MMSE method of [8] works well for an elevation range from $-90°$ to 90°; however, it gives much worse results than the other methods for a narrower range of elevation, e.g., from $-30°$ to 90°, particularly at the extreme elevations (below 0° and beyond 60°), as shown in Fig. 12 for the first range bin. This is because the MMSE method suffers from a lack of convergence when the range of elevation is shrunk. Fig. 13 shows a close-up of range–elevation cross section of reflectivity for the four methods in elevations from $-10°$ to 10° with 0.1° spacing and 100 range bins (a total distance of 10 km) at 0° azimuth. The output clutter levels were 13.91, 9.73, 8.17, and 5.54 dB, for FR, MMSE, FPA, and RBFNN, respectively. This comparison clearly illustrates

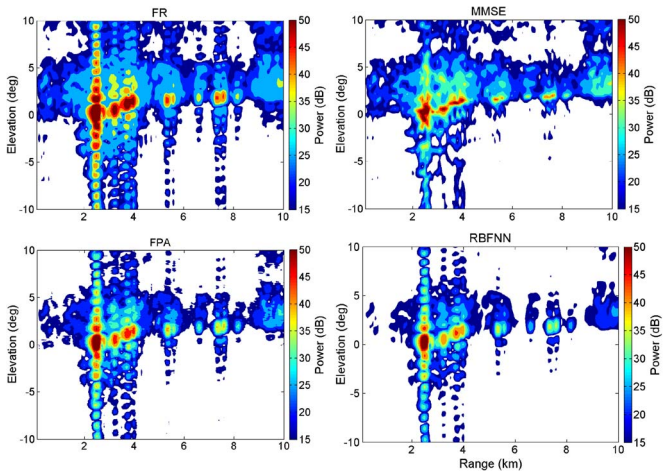

Fig. 13. Range–elevation cross sections of reflectivity based on data collected by the PAR@OU at 0° azimuth.

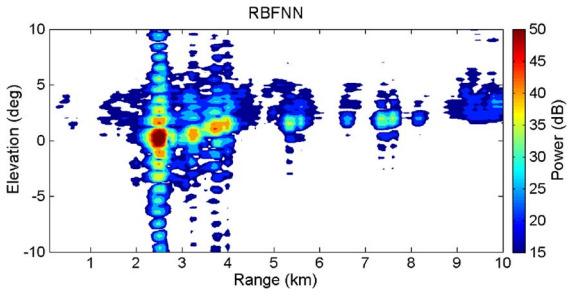

Fig. 14. Range–elevation cross sections of reflectivity of PAR@OU for the RBFNN trained with 0.5° elevation step and tested with 0.1° step.

that the RBFNN correctly detects precipitation profiles with the least clutter. The RBFNN training time was 4 s per range bin (about 7 min for a 10-km range) using 201 epochs (or hidden nodes) for a goal MSE of 1.0E-7 and a spread parameter of 1.

Average CPU time taken per range bin per elevation angle was 63 μs, 0.1, 0.14, and 0.6 s, for FR, RBFNN, MMSE, and FPA, respectively. Again, FR is the fastest beamformer among all, and RBFNN is six times faster than FPA and about one and half faster than MMSE.

Fig. 14 shows the range–elevation cross section of reflectivity of the RBFNN beamformer trained with 0.5° elevation step and tested with 0.1° step. The clutter level in this case is 4.86 dB, and the total training time is 28 s.

V. Conclusion

In this paper, we have proposed a RBFNN-based beamformer for phased array weather radar. The performance of the RBFNN beamformer is evaluated for the point targets such as aircrafts and missiles and the distributed targets such as precipitation. Performance was validated by numerically simulated precipitation data, which has narrow-band random signals whose Doppler spectrum is Gaussian shaped. Simulation results indicate that the RBFNN algorithm adaptively suppresses sidelobes and correctly estimates power; it has also been shown that its performance is superior to that of the FR, CP, and FPA methods. Moreover, the RBFNN has shown excellent performance even with 16 pulses; additionally, it is anticipated that strong ground clutter contaminates the desired distributed signals because the PAR is designed to be installed in an urban area. In the numerical simulations with strong ground clutter, the RBFNN has shown performance as good as without ground clutter. Evaluation with real data obtained by the PAR@OU was also carried out, where the RBFNN is shown to be appropriate for real-time beamforming of PAR@OU, which requires around 16 pulses per single direction in order to scan rapidly. The RBFNN estimated PAR@OU reflectivity with less clutter than FR, MMSE, and FPA, taking about 4 s training time per range bin. These results indicate that this RBFNN approach can be applied to pulse compression weather radars for ranging with high resolution [20].

Acknowledgment

The authors would like to thank Prof. V. Chandrasekar at Colorado State University for providing the radar signal simulator and Dr. E. Yoshikawa at the Japan Aerospace Exploration Agency (JAXA) for the helpful discussions.

References

[1] A. L. Pazmany and H. B. Bluestein, "Mobile rapid-scanning X-band polarimetric (RaxPol) Doppler radar," in *Proc. 35th Conf. Radar Meteorol.*, Pittsburgh, PA, USA, 2011, pp. 1–5.

[2] B. Isom *et al.*, "The atmospheric imaging radar: Simultaneous volumetric observations using a phased array weather radar," *J. Atmos. Ocean. Technol.*, vol. 30, no. 4, pp. 655–675, Apr. 2013.

[3] J. Vivekanandan *et al.*, "The next generation airborne polarimetric Doppler weather radar," *Geosci. Instrum. Methods Data Syst.*, vol. 3, pp. 111–126, 2014.

[4] D. S. Zrnic *et al.*, "Agile-beam phased array radar for weather observations," *Bull. Amer. Meteorol. Soc.*, vol. 88, no. 11, pp. 1753–1766, Nov. 2007.

[5] F. Mizutani *et al.*, "Development of active phased array weather radar," in *Proc. 35th Conf. Radar Meteorol.*, Pittsburgh, PA, USA, 2011, pp. 1–6.

[6] R. D. Palmer, S. Gopalam, T.-Y. Yu, and S. Fukao, "Coherent radar imaging using Capon's method," *Radio Sci.*, vol. 33, no. 6, pp. 1585–1598, Nov./Dec. 1998.

[7] B. L. Cheong, M. W. Hoffman, R. D. Palmer, S. J. Frasier, and F. J. Lopez-Dekker, "Pulse pair beamforming and the effects of reflectivity field variations on imaging radars," *Radio Sci.*, vol. 39, no. 3, pp. 1–13, Jun. 2004.

[8] E. Yoshikawa *et al.*, "MMSE beam forming on fast-scanning phased array weather radar," *IEEE Trans. Geosci. Remote Sens.*, vol. 51, no. 5, pp. 3077–3088, May 2013.

[9] S. Haykin, *Neural Network: A Comprehensive Foundation*. Upper Saddle River, NJ, USA: Prentice-Hall, 1999.

[10] A. H. El Zooghby, C. G. Christodoulou, and M. Georgiopoulos, "Performance of radial-basis function networks for direction of arrival estimation with antenna arrays,"*IEEE Trans. Antennas Propag.*, vol. 45, no. 11, pp. 1611–1617, Nov. 1997.

[11] Y. Liu, J. Xia, Y. Hong, and C. X. Shi, "An improved cloud classification algorithm for China's FY-2C multi-channel images using artificial neural network," *Sensors*, vol. 9, pp. 5558–5579, 2009.

[12] W. Blackwell, "A neural-network technique for the retrieval of atmospheric temperature and moisture profiles from high spectral resolution sounding data," *IEEE Trans. Geosci. Remote Sens.*, vol. 43, no. 11, pp. 2535–2546, Nov. 2005.

[13] H. Liu, V. Chandrasekar, and G. Xu, "An adaptive neural network scheme for radar rainfall estimation from WSR-88D observations," *J. Appl. Meteorol.*, vol. 40, no. 11, pp. 2038–2050, 2001.

[14] C. A. Balanis and P. I. Ioannides, *Introduction to Smart Antennas*. San Rafael, CA, USA: Morgan & Claypool, 2007.

[15] X.-S. Yang, "Flower pollination algorithm for global optimization," in *Unconventional Computation and Natural Computation*, ser. Lecture Notes in Computer Science, vol. 7445. Berlin, Germany: Springer-Verlag, 2012, pp. 240–249.

[16] I. Pavlyukevich, "Lévy flights, non-local search and simulated annealing," *J. Comput. Phys.*, vol. 226, no. 2, pp. 1830–1844, 2007.

[17] K.-L. Du, K. K. Cheng, and M. N. Swamy, "A fast neural beamformer for antenna arrays," in *Proc. IEEE Int. Conf. Commun.*, New York, NY, USA, Apr./May 2002, pp. 139–144.
[18] V. Chandrasekar, V. N. Bringi, and P. Brockwell, "Statistical properties of dual-polarized radar signals," in *Proc. 23rd Conf. Radar Meteorol.*, Snowmass, CO, USA, 1986, pp. 193–196.
[19] V. N. Bringi and V. Chandrasekar, *Polarimetric Doppler Weather Radar: Principles and Applications*. Cambridge, U.K.: Cambridge Univ. Press, 2001, pp. 222–232.
[20] D. V. Chandrasekar *et al.*, "Scientific and engineering overview of the NASA Dual-frequency Dual-polarized Doppler Radar (D3R) system for GPM ground validation," in *Proc. IEEE Int. Geosci. Remote Sens. Symp.*, Honolulu, HI, USA, 2010, pp. 1308–1311.

Tarek Sallam was born in Cairo, Egypt, in 1982. He received the B.S. degree in electronics and telecommunications engineering and the M.S. degree in engineering mathematics from Banha University, Cairo, Egypt, in 2004 and 2011, respectively, and the Ph.D. degree in electronics and communications engineering from Egypt–Japan University of Science and Technology, New Borg El-Arab City, Egypt, in 2015.

From 2005 to 2006, he was a Researcher Assistant with the High Frequency Lab, National Institute of Standards, Giza, Egypt. Since 2006, he has been with the Department of Engineering Mathematics and Physics, Faculty of Engineering at Shoubra, Banha University, where he is currently an Assistant Professor. From August 2014 to May 2015, he was a Visiting Researcher with the Electromagnetic Compatibility Lab, Department of Information and Communications Technology, Graduate School of Engineering, Osaka University, Osaka, Japan. His research interests include evolutionary optimization, artificial neural networks, phased array antennas with array signal processing and adaptive beamforming, and phased array radar with weather radar as a special case.

Adel B. Abdel-Rahman was born in Aswan, Egypt, in 1968. He received the B.S. and M.S. degrees in electrical engineering, communication, and electronics from Assuit University, Assuit, Egypt, in 1991 and 1998, respectively, and the Doktor-Ing. degree in communication engineering from Magdeburg University, Magdeburg, Germany, in 2005.

Since May 2010, he has been the Executive Director for Information and Communication Technology, South Valley University, Qena, Egypt. Since October 2012, he has been an Associate Professor with the School of Electronics, Communications and Computer Engineering, Egypt–Japan University of Science and Technology, Alexandria, Egypt. He is currently with the Department of Electrical Engineering, South Valley University. He is the author or coauthor of over 60 papers in international journals and proceedings of international and national symposia. His research interests include the design and analysis of antennas, filters, metamaterials, and its applications in wireless communication, and optimization techniques with applications to microwave passive devices and antenna arrays.

Dr. Abdel-Rahman is a Reviewer for IEEE MICROWAVE AND WIRELESS COMPONENTS LETTERS.

Masoud Alghoniemy (SM'14) received the B.S. and M.S. degrees from the University of Alexandria, Alexandria, Egypt, and the Ph.D. degree from the University of Minnesota, Minneapolis, MN, USA, in 1993, 1996, and 2001, respectively.

From March 2010 to July 2010, he worked as a Senior Research Scientist with Intel Corporation, Egypt, where he worked on IEEE 802.16m mobile WiMAX standard. From 2010 to 2012, he was an Associate Professor with the Egypt–Japan University of Science and Technology, Alexandria. In the summer of 2000, he was also with Intel Corporation, Santa Clara, CA, USA. He is currently an Associate Professor with the Department of Electrical Engineering, University of Alexandria. From April 2001 to March 2002, he was a Senior Audio Coding Engineer with iBiquity Digital Corporation, Warren, NJ, USA. His research interests include convex optimization in signal processing and sparse signal representations. From October 2006 to October 2008, he was with the Malaysian Institute of Microelectronic Systems (MIMOS BHD), Malaysia, where he was part of a team responsible for implementing the physical layer of the WiMAX standard IEEE 802.16e.

Dr. Alghoniemy received the Young Scientist Award from the General Assembly of the International Union of Radio Science, Lille, France, in 1996 and the State Incentive Award for Engineering Sciences from the Academy of Scientific Research, Egypt, in 2014.

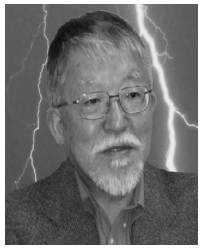

Zen Kawasaki (M'72) received the B.S., M.S., and Dr. Eng. degrees from Osaka University, Osaka, Japan, in 1973, 1975, and 1978, respectively, all in communications engineering.

From 1989 to 2013, he was with the Division of Electrical, Electronic and Information Engineering, Osaka University. From 2010 to 2012, he was the Dean Advisor of the Egypt–Japan University of Science and Technology, Alexandria, Egypt. His research interests include electromagnetic compatibility and atmospheric electricity.

Dr. Kawasaki served as the President of the International Commission on Atmospheric Electricity (ICAE) from 2007 to 2014. He received the Institute of Electrical Engineers of Japan (IEEJ) Technical Progress Award for the Success of Laser Triggered Lightning in the Field Experiment, the Laser Institute of Technology Technical Progress Award for the Success of Laser Triggered Lightning in the Field Experiment, the IEEJ Technical Progress Award for the Success of Maido Micro-Lab Satellite, and the IEEJ paper Award on VHF Broadband interferometry. He is currently a member of ICAE, American Geophysical Union, and IEICE Japan, and a Fellow of IEEJ.

Tomoo Ushio (M'00) received the B.S., M.S., and Ph.D. degrees from Osaka University, Osaka, Japan, in 1993, 1995, and 1998, respectively, all in electrical engineering.

From 1998 to 2000, he was with the Global Hydrology and Climate Center, Huntsville, AL, USA, as a Postdoctorate Researcher. Since 2000, he has been with the Department of Aerospace Engineering, Osaka Prefecture University, Osaka, Japan. After being an Assistant Professor with Osaka Prefecture University in 2006, he joined the Division of Electrical, Electric and Information Engineering, Osaka University, where he is currently an Associate Professor. His research interests include radar-based remote sensing, passive and active remote sensing of atmosphere from spaceborne platforms, and atmospheric electricity.